RESEARCH ARTICLE

An ultra-sensitive electrochemical sensor based on MOF-derived ZnO/Co$_3$O$_4$ decorated on graphene for low-level monitoring of the α$_1$-AR antagonist alfuzosin in tablets and human samples†

Gajapaneni Venkata Prasad, [ID] Venkatachalam Vinothkumar, [ID] Seung Joo Jang [ID] and Tae Hyun Kim [ID] *

We present a novel electrochemical sensor for the detection of alfuzosin (AFZ), an alpha1-adrenoceptor (α$_1$-AR) antagonist using metal−organic framework (MOF)-derived zinc oxide/cobalt oxide (ZnO/Co$_3$O$_4$) decorated on graphene (Gr). The co-precipitation method was utilized to synthesize a binary metal oxide derived from the MOF, and then ultrasonication was employed to prepare the ZnO/Co$_3$O$_4$@Gr nanocomposite. The prepared ZnO/Co$_3$O$_4$@Gr nanocomposite was characterized by X-ray diffraction (XRD), X-ray photoelectron spectroscopy (XPS), attenuated total reflectance-infrared (ATR-IR) spectroscopy, field emission scanning electron microscopy (FE-SEM), and high-resolution transmission electron microscopy (HR-TEM). The nanocomposite was modified on a glassy carbon electrode (GCE) to construct an electrochemical AFZ sensor, which exhibited a linear range of 0.05−40 μM and a low limit of detection (LOD) of 0.004 μM. The sensor showed good selectivity, as well as excellent reproducibility and storage stability. We also conducted the real sample analysis of the modified electrode for the detection of AFZ in pharmaceutical tablets, human serum, and urine samples, which delivered adequate recoveries. The ZnO/Co$_3$O$_4$@Gr nanocomposite-based electrochemical sensor is a promising candidate for the efficient and accurate detection of AFZ, owing to its superior sensitivity, selectivity, reproducibility, and stability.

1. Introduction

Benign prostatic hyperplasia (BPH) is a noncancerous growth of the prostate gland that commonly affects men, obstructing the passage of urine and causing bladder and urinary tract infections and kidney disorders. Alpha-adrenergic blockers are the current standard of care for BPH treatment, with alfuzosin hydrochloride (AFZ) being a commonly prescribed medication.[1] AFZ is a second-generation alpha1-adrenoceptor (α$_1$-AR) antagonist, which means that it blocks the action of the α$_1$-adrenergic receptors. These receptors are located in the smooth muscles of the bladder neck and prostate gland. By blocking these receptors, AFZ relaxes the smooth muscles and allows urine to flow more freely.[2,3] AFZ is generally well-tolerated, but it can cause side effects such as dizziness, headache, and hypotension. In rare cases, AFZ can also cause more serious side effects, such as orthostatic hypotension, priapism, and hypersensitivity reactions. Because of the potential for

side effects, it is important to monitor AFZ levels in patients who are taking this medication. It has been suggested that uric acid (UA) lowering medications could potentially decrease urinary symptoms associated with BPH and could potentially reduce the need for traditional BPH drugs like alpha-blockers.[4] BPH is more common in men with higher UA and gout, especially young males with gout. Excessive UA in BPH patients can cause tissue injury, inflammation, and deposition, leading to a lower prostate-specific antigen (PSA) ratio.[5] For these reasons, it is important to consider the potential side effects of AFZ and monitor patients closely, especially those with high UA levels or a history of gout, in order to optimize their treatment for BPH. The selective detection of AFZ in the presence of UA is a challenging task for researchers. Various analytical methods, such as chromatographic,[6] conductometric,[7] potentiometric,[8] and spectrophotometric methods,[9] have been proposed for detecting AFZ. Despite their effectiveness, these methods are expensive and necessitate complicated chemical processes that are often time-consuming and tedious and require a skilled analyst to handle their equipment. Additionally, they do not provide insights into the pharmacological activity or response mechanism of the drug. In contrast, electrochemical approaches have garnered signifi-

Department of Chemistry, Soonchunhyang University, Asan, 31538, Republic of Korea. E-mail: thkim@sch.ac.kr

This journal is © the Partner Organisations 2023

Inorg. Chem. Front., 2023, **10**, 4829–4844 | **4829**

cant attention due to their quick response time, low cost, high sensitivity, ease of handling, and economic feasibility.[10] Furthermore, these approaches have considerable potential for examining the redox reaction of drugs and delivering essential pharmacological and pharmacokinetic insights. However, there are still limited reports on the application of electro-chemical approaches for determining AFZ. Therefore, there is a growing need to develop a simple, inexpensive, and sensitive electrochemical sensor for detecting AFZ. To our knowledge, only a few electrochemical techniques using modified and unmodified glassy carbon electrodes have been used for the electrochemical oxidation of AFZ.[11–13]

Researchers have been interested in developing innovative electrochemical sensors that leverage the superior features of nanomaterials. Nanoparticles (NPs) have attracted a lot of attention due to their exceptional physical, chemical, optical, and electrical properties compared to bulk materials.[14] Recently, transition-metal oxide (TMO) nanostructures have garnered a lot of attention for their excellent performance in various fields, including electrical, magnetic, and optical applications. TMO NPs have many distinctive features, including a large band gap, favorable electrical properties, high dielectric constants, and reactive electronic transitions.[15,16] Among several transition metal oxides, cobalt oxide (Co_3O_4) is a well-known p-type semiconductor with an indirect band gap in the range from 1.6 to 2.2 eV. It has a typical AB_2O_4 cubic spinal structure, with Co^{2+} ions occupying the tetrahedral sites and Co^{3+} ions occupying the octahedral sites. Oxygen molecules can be readily adsorbed on the surface of Co_3O_4 due to the ease with which Co^{2+} ions can be oxidized to higher oxidation states.[17] Moreover, Co_3O_4 is an intriguing material for sensing applications owing to the redox behavior of the Co^{2+}/Co^{3+} interaction.[18–20] On the other hand, zinc oxide (ZnO) is an n-type semiconducting oxide material with a wide band gap of 3.37 eV and a high excitation binding energy of 60 meV.[21] ZnO is eco-friendly, abundant on earth, low-cost to synthesize, and can produce electron–hole pairs when exposed to visible or UV light. These properties have led to ZnO being considered a viable electrode material.[22] However, ZnO has some limitations such as low conductivity and poor stability, which restrict its potential for sensing application. To overcome these limitations, we propose combining ZnO and Co_3O_4 to form a p–n heterojunction. A p–n heterojunction is a junction between two semiconductor materials with different band gaps. This junction creates a depletion region, where there are no free charge carriers. Also, this depletion region can act as a barrier to the flow of charge carriers, which can provide exceptional sensing application capabilities. The combination of ZnO and Co_3O_4 could improve the selectivity and conductivity of ZnO. This is because Co_3O_4 can act as a catalyst for the oxidation of analytes, while ZnO can act as a conductor for the electrons generated by the oxidation reaction. The development of electrochemical sensors based on p–n heterojunction is a promising area of research. These sensors have the potential to be more sensitive, selective, and cost-effective than traditional electrochemical sensors.

Metal–organic frameworks (MOFs) are a unique class of porous crystalline materials with exceptional properties, such as open metal sites, organic linkers, tunable functions, high surface areas, and thermal stability.[23] These properties have led to a wide range of applications for MOFs in gas sensing,[24] energy storage,[25] drug delivery,[26] and electrocatalysis.[27] MOFs have also been recognized as potential candidates for electro-chemical sensor materials due to their excellent structural characteristics.[28–30] However, when utilized as electrode materials for the construction of electrochemical sensors, MOFs have several drawbacks, including poor electrocatalytic activity, low electronic conductivity, and reduced mechanical strength. These drawbacks limit the sensitivity and stability of MOF-based electrochemical sensors.[31] Hence, improving the stability and electrical conductivity of MOFs is critical for expanding their use in electrochemical applications. Several innovative MOF-based composites have been developed in recent years for electrochemical sensing applications. These include MOF-derived porous $ZnO-Co_3O_4$ nanocages for the colorimetric determination of copper ions,[32] ZnO@ZIF-8 nano-composites for the selective detection of hydrogen peroxide and ascorbic acid,[33] MOF-derived NiO@ZnO for the detection of isoniazid,[34] MOF-derived $PdNPs@ZnO-Co_3O_4$-MWCNTs for the detection of the tanshinol drug,[35] MOF-derived $ZnO-Co_3O_4@C_3N_4$ for the detection of flutamide,[36] and MOF-derived binary metal oxide NiO@ZnO for the detection of rutin.[21] Also, some reports are available in MOF-derived ZnO/Co_3O_4 for ethanol gas sensing[37] and MOF-derived ZnO/Co_3O_4 hetero-nanostructures for photocatalytic applications.[38] To further improve the electrochemical performance of MOFs, highly conductive graphene (Gr) has been included in MOFs. Gr has received a great deal of interest in the field of electro-chemical sensors due to its superior physical and chemical characteristics, including a considerable surface area, good electrical conductivity, and strong electrocatalytic activity.[39,40] In Gr-based MOF hybrids, Gr not only improves the electrical conductivity and mechanical strength, but also markedly enhances the stability and electrochemical catalytic activity of fabricated electrodes.[41] The active synergistic functionality of MOFs@Gr hybrids has resulted in an improvement in electro-chemical performance. Furthermore, the π–π stacking interaction between the imidazole groups of the ligands in MOFs and Gr can enhance the electron mobility by delocalizing electrons across the entire conjugated composite.[42,43]

In this research, a bimetallic zeolitic imidazole framework based on zinc cobalt (ZIF-ZnCo) was synthesized and used as a self-sacrificing template to construct a ZnO/Co_3O_4 composite. The bimetallic ZIF-ZnCo composite was synthesized using a simple and inexpensive co-precipitation process. During calcination, the bimetallic template ZIF-ZnCo was transformed into highly porous ZnO/Co_3O_4 via the Kirkendall effect. However, at high operating temperatures, the catalyst ZnO/Co_3O_4 easily aggregates, which significantly deteriorates the sensing characteristics. To overcome this issue, we synthesized nanoscale catalysts by incorporating Gr sheets via a simple sonochemical approach. The resulting ZnO/$Co_3O_4@Gr$ nanocomposite was

4830 | *Inorg. Chem. Front.*, 2023, **10**, 4829–4844

This journal is © the Partner Organisations 2023

dropped on a glassy carbon electrode to create a modified electrode (denoted as ZnO/Co$_3$O$_4$@Gr/GCE) which was used for the ultrasensitive detection of AFZ in biological fluids for the first time. The results demonstrated that the α$_1$-adrenergic receptor antagonist AFZ drug had well-separated and increased oxidation peaks on the modified electrode, opening up a new avenue for the prospective electrochemical application of the MOF materials. This research provides a theoretical and practical basis for constructing highly dispersible and stable MOF@Gr-based composites and highlights their promising electrochemical applications.

2. Experimental

ESI (S1–S4†) provides details about the chemicals, equipment, electrochemical measurements, and preparation of real samples.

2.1. Synthesis of ZIF-Zn or ZIF-Co

A simple co-precipitation reaction procedure at ambient temperature was used to synthesize ZIF-Zn or ZIF-Co. In a typical synthesis, 1.98 mmol of Zn(NO$_3$)$_2$·6H$_2$O or 1.60 mmol of Co (NO$_3$)$_2$·6H$_2$O and 15.83 mmol of 2-methylimidazole (2-MIM) were first individually diluted in methanol (40 mL) and subjected to ultrasonication followed by magnetic stirring to form a clear solution. After stirring for 30 min, the clear 2-MIM solution was added slowly, dropwise, to the Zn(NO$_3$)$_2$·6H$_2$O or Co (NO$_3$)$_2$·6H$_2$O solution. The mixture was then left static for 24 hours at room temperature. The resulting mixture was centrifuged and washed multiple times with methanol followed by vacuum drying at 80 °C for a period overnight. Finally, the obtained product was described to be ZIF-Zn (called ZIF-8) or ZIF-Co (called ZIF-67).

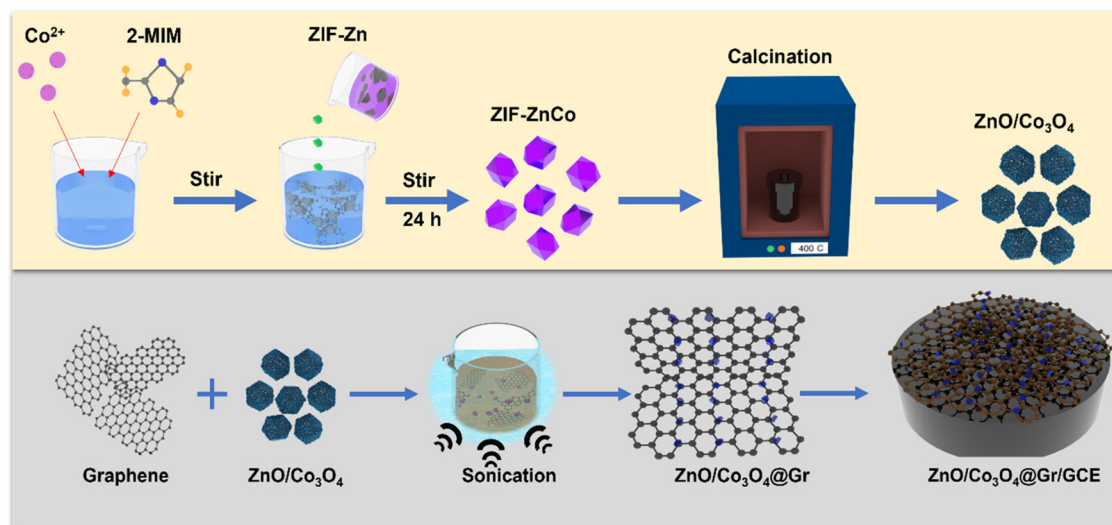### 2.2. Synthesis of bimetallic ZIF-ZnCo

As-synthesized ZIF-Zn was used as a template to create bimetallic ZIF-ZnCo. In a typical synthesis, 1.60 mmol of Co (NO$_3$)$_2$·6H$_2$O and 15.83 mmol of 2-MIM were first individually diluted in methanol (40 mL) and subjected to ultrasonication followed by magnetic stirring to form a clear solution. Next, 0.2 g of ZIF-Zn was added to the cobalt source solution while stirring vigorously. The 2-MIM solution was then added dropwise to the ZIF-Zn solution, and the stirring was continued. The mixture was left static for 24 hours at room temperature. The resulting mixture was centrifuged and washed multiple times with methanol followed by vacuum drying at 80 °C overnight. Finally, the obtained product was described to be bimetallic ZIF-ZnCo.

2.3. Synthesis of ZnO, Co$_3$O$_4$, ZnO/Co$_3$O$_4$ and ZnO/Co$_3$O$_4$@Gr nanocomposite

The synthesized ZIF-Zn, ZIF-Co, and bimetallic ZIF-ZnCo powders were calcined at 400 °C for 2 h at a heating rate of 2 °C min^{-1} in air to produce ZnO, Co$_3$O$_4$, and ZnO/Co$_3$O$_4$ composite, respectively. To prepare the ZnO/Co$_3$O$_4$@Gr nanocomposite, 10 mg of Gr was dispersed in ethanol by ultrasonication for 30 min at room temperature and centrifuged at 5000 rpm for 15 min. Then, 10 mg of the ZnO/Co$_3$O$_4$ powder was added to the 10 mg/10 mL Gr solution and ultrasonicated for 30 min. The weakly bound Gr and ZnO/Co$_3$O$_4$ particles were removed by centrifugation at 5000 rpm for 15 min. After multiple washes in deionized water and ethanol, the obtained product was dried for 5 h at 80 °C to furnish the ZnO/Co$_3$O$_4$@Gr nanocomposite. Scheme 1 depicts a graphical illustration of the synthesis of the ZnO/Co$_3$O$_4$@Gr nanocomposite.

2.4. Preparation of working electrodes

Prior to modifying the working electrode, the glassy carbon electrode (GCE) was sequentially polished with alumina

Scheme 1 Graphical illustration for the preparation of the ZnO/Co$_3$O$_4$@Gr nanocomposite.

powders of various sizes, including 0.1, 0.3, and 0.05 μm, respectively. The electrode was then cleaned multiple times using deionized water and ethanol by ultrasonication. To prepare a ZnO/Co$_3$O$_4$@Gr dispersion, 1 mg of the ZnO/Co$_3$O$_4$@Gr nanocomposite was dispersed in 1 mL of methanol and homogenized by ultrasonication and vortex mixing. The cleaned GCE surface was then immobilized with 5 μL of the ZnO/Co$_3$O$_4$@Gr suspension and allowed to dry under an IR lamp. The modified GCE was designated as ZnO/Co$_3$O$_4$@Gr/GCE and subsequently used as a non-enzymatic electrochemical sensor for detecting AFZ. Similarly, ZnO/GCE, Co$_3$O$_4$/GCE, and ZnO/Co$_3$O$_4$/GCE were constructed using similar procedures.

3. Results and discussion

3.1. Structural investigations

To verify the structural integrity and composition of the synthesized catalysts, X-ray diffraction (XRD) studies were conducted. Fig. S1† shows the XRD patterns of ZIF-Zn and ZIF-Co crystals, which exhibit the diffraction peaks at 7.43°, 10.42°, 12.79°, 14.75°, 16.50°, 18.11°, 22.18°, 24.56°, and 26.75° corresponding to the (011), (002), (112), (022), (013), (222), (114), (233), and (134) planes, respectively.[44] Notably, no additional peaks were observed when comparing the diffraction peaks of the parent ZIFs to those of the bimetallic ZIF-ZnCo. This suggests that the inherent framework structure of the parent ZIFs was sustained throughout the formation of the composite. Furthermore, there was no segregation of the ZIF-Zn and ZIF-Co crystals in the composite's diffraction peaks, which is likely due to the similar ionic radii (0.74 A°

and 0.72 A°, respectively) of Zn^{2+} and Co^{2+} in the tetrahedral coordination, allowing Co^{2+} ions to replace Zn^{2+} ions.[45] Fig. 1a displays the characteristic XRD patterns of ZnO, Co$_3$O$_4$, ZnO/Co$_3$O$_4$, and ZnO/Co$_3$O$_4$@Gr nanocomposite after the calcination of all ZIFs. The XRD spectrum of Gr shows diffraction peaks at 2θ = 25.5° and 43°, which correspond to the (002) and (101) planes, respectively. This indicates that the Gr is in the graphitic phase. The ZnO diffraction peaks at 2θ = 31.70°, 34.25°, 36.09°, 47.35°, 56.49°, 62.78°, and 67.76° correspond to the (100), (002), (101), (102), (110), (103), and (112) planes of ZnO (JCPDS Card 36-1451), respectively. The Co$_3$O$_4$ diffraction peaks at 2θ = 19.14°, 31.37°, 36.92°, 44.90°, 59.50°, and 65.30° correspond to the (111), (220), (311), (400), (511), and (440) planes of Co$_3$O$_4$ (JCPDS Card 65-3103), respectively. The XRD characterization of ZnO/Co$_3$O$_4$ revealed no distinctive peaks for ZnO or Co$_3$O$_4$, nor were any impure peaks present, representing that the precursors ZIF-Zn, ZIF-Co, and bimetallic ZIF-ZnCo were completely converted into ZnO, Co$_3$O$_4$, and ZnO/Co$_3$O$_4$. The faint hump at about 2θ = 25.5° in the XRD pattern of ZnO/Co$_3$O$_4$@Gr indicates the presence of carbon. The fact that the diffraction peaks of the other components remain in the same orientation after the addition of Gr indicates that the addition of Gr did not significantly change the crystal structure of the nanocomposite.[46]

Attenuated total reflectance infrared (ATR-IR) spectroscopy was also used to confirm the structural validation of the produced catalysts. Fig. S2a† depicts the coordination of the organic ligand (2-MIM) with the metals (Co/Zn) from ATR-IR spectra of 2-MIM ligand, ZIF-Co, ZIF-Zn, and bimetallic ZIF-ZnCo. As can be seen in Fig. S2a,† the 2-MIM ligand exhibited a single broad peak from 2300 to 3100 cm^{-1}, which is attributed to the N–H–N hydrogen bond identified between

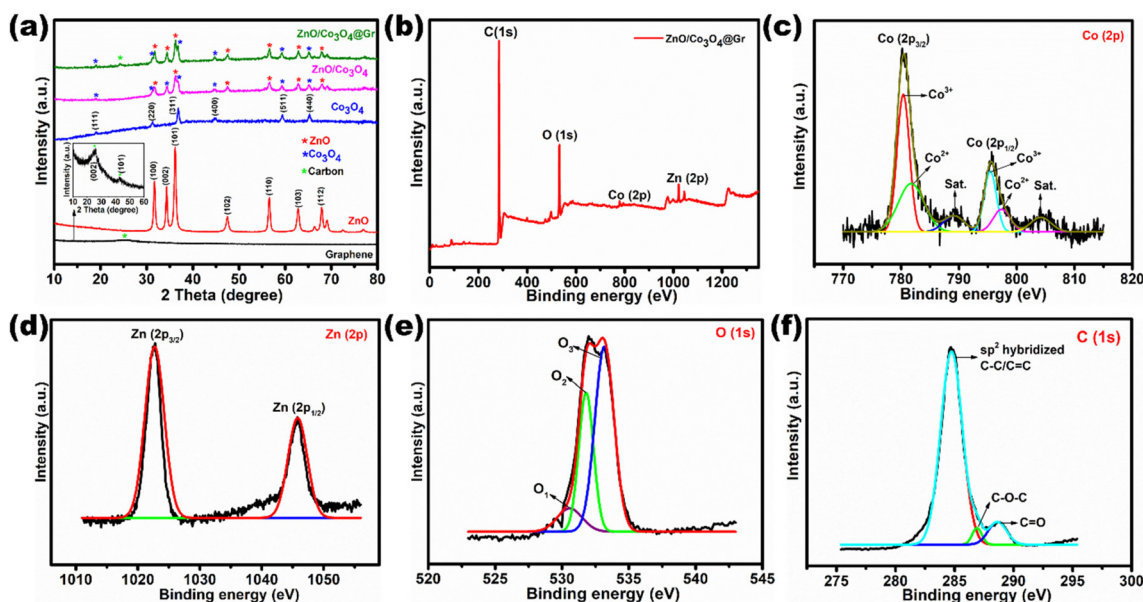**Fig. 1** (a) XRD patterns of Gr, ZnO, Co$_3$O$_4$, ZnO/Co$_3$O$_4$, and the ZnO/Co$_3$O$_4$@Gr nanocomposite, (b–f) XPS analysis of ZnO/Co$_3$O$_4$@Gr: (b) full survey and high resolutions of (c) Co 2p, (d) Zn 2p, (e) O 1s, and (f) C 1s, respectively.

the two 2-MIM ligands. A peak was also observed at 1835 cm^{-1}, which was associated with the N–H stretching vibration. The two adsorption bands mentioned completely vanished in the spectra of as-prepared ZIF-Co, ZIF-Zn, and bimetallic ZIF-ZnCo, indicating that the N–H groups of the 2-MIM ligands were deprotonated following coordination with the Co^{2+}/Zn^{2+} ions. The peaks for out-of-plane vibrations and C=N stretching vibrations in each of the three ZIFs were 1573 cm^{-1} and 755 cm^{-1}, respectively. In addition, a novel adsorption peak at 424 cm^{-1} developed in all three ZIFs, demonstrating the metal–nitrogen (–M–N) stretching mode.[47] The ATR-IR investigation results demonstrate the coordination between the metal clusters and organic linkers in the framework. It was also evident that bimetallic ZIF-ZnCo was synthesized while Zn/Co was concurrently incorporated into the framework. Interestingly, after calcining all ZIFs at 400 °C for 2 h, all these strong and weak peaks vanished, implying the development of metal oxide hetero nanostructures, as depicted in Fig. S2b.† Fig. S2b† shows the structural evidence for the as-synthesized ZnO, Co$_3$O$_4$, ZnO/Co$_3$O$_4$, and ZnO/Co$_3$O$_4$@Gr nanocomposite. The peak at 526 cm^{-1} in the ATR-IR spectra was ascribed to the Zn–O stretching mode, confirming the formation of ZnO. The peaks at 554 cm^{-1} and 662 cm^{-1} in the spectrum of Co$_3$O$_4$ correspond to the Co–O stretching mode, which assisted in the formation of Co$_3$O$_4$.[48] The addition of Gr did not affect the peaks in the ZnO/Co$_3$O$_4$@Gr nanocomposite. Furthermore, X-ray photoelectron spectroscopy (XPS) was performed to identify the oxidation states, chemical composition, and interactions in the developed nanocomposite. Fig. 1b shows the XPS analysis spectrum of the ZnO/Co$_3$O$_4$@Gr nanocomposite, covering the full survey scanning range. The spectrum reveals the presence of chemical components Co, Zn, O, and C in the composite. No additional elements were detected, showing the high purity of the sample, consistent with XRD and EDS analysis. The high-resolution XPS spectrum of Co 2p (Fig. 1c) displays two prominent peaks at binding energies of 780.41 eV and 795.75 eV, corresponding to Co 2p$_{3/2}$ and Co 2p$_{1/2}$ peaks, respectively. The spin energy separation between the Co 2p$_{3/2}$ and Co 2p$_{1/2}$ peaks was 15.35 eV, confirming the presence of Co^{3+} and Co^{2+} in the composite.[37] Further confirmation of the existence of Co$_3$O$_4$ in the composite was provided by the presence of Co^{3+} (780.27 eV) and Co^{2+} (781.21) in the strong peak of Co 2p$_{3/2}$, and the presence of Co^{3+} (795.18 eV) and Co^{2+} (796.90 eV) in the shoulder peak of Co 2p$_{1/2}$, respectively.[49] Two faint shake-up satellite peaks with binding energies of 789.17 eV and 804.40 eV were also observed, corresponding to the Co 2p$_{3/2}$ and Co 2p$_{1/2}$ peaks, respectively. The high-resolution XPS spectrum of Zn 2p (Fig. 1d) shows two distinct peaks at binding energies of 1022.67 eV and 1045.77 eV, attributed to the Zn 2p$_{3/2}$ and Zn 2p$_{1/2}$ peaks. The spin orbital splitting of two energy levels (Zn 2p$_{3/2}$ and Zn 2p$_{1/2}$) is at 23.1 eV,[50] demonstrating the presence of Zn^{2+} in the prepared composite. The O 1s high-resolution XPS spectrum (Fig. 1e) revealed the presence of O$_1$, O$_2$, and O$_3$ with binding energies of 530.17, 531.73, and 533.14 eV, respectively. These are due to Co–O, Zn–O, and H–O–H bonds in surface hydroxides.[51] The C

1s peak in high-resolution XPS spectra (Fig. 1f) contains three Gaussian peaks at the binding energies of 284.77, 286.34, and 288.71 eV, attributed to sp^2 hybridized C–C/C=C, C–O–C, and C=O groups in the composite.[52] Table 1 summarizes the XPS data of the ZnO/Co$_3$O$_4$@Gr nanocomposite.

3.2. Surface morphological investigations

The surface morphology of as-synthesized MOF catalysts was investigated using field emission scanning electron microscope (FE-SEM) and field emission transmission electron microscope (FE-TEM) analyses. FE-SEM images of as-synthesized MOF catalysts such as ZIF-Zn and ZIF-Co revealed rhombic dodecahedron morphologies with smooth surfaces (Fig. S3a and b†), consistent with the previous literature.[53,54] The surface morphology of the bimetallic ZIF-ZnCo composite changed from smooth to rough surfaces, indicating successful composite formation (Fig. S3c†). In addition, a minimal number of large-sized ZIF-Co particles were formed on the surface of ZIF-Zn, as shown in Fig. S3c.† The elemental composition of ZIF-Zn, ZIF-Co, and bimetallic ZIF-ZnCo was confirmed by energy dispersive spectroscopy (EDS) analysis (Fig. S3d–f†). Elemental mapping also further confirmed the successful formation of the bimetallic ZIF-ZnCo (Fig. S3g–k†). Calcination of the precursors (ZIF-Zn, ZIF-Co, and bimetallic ZIF-ZnCo) at 400 °C resulted in the formation of MOF-derived oxides with different morphologies. After calcination, the surface morphologies of the precursors were significantly altered from smooth to rough and porous, as seen in Fig. 2a–c. The MOF-derived ZnO nanomaterial retained its dodecahedral structure after calcination, but its size was smaller than that of the ZIF-Zn precursor due to decomposition.[55] EDS measurements confirmed the presence of existing elements in ZnO, Co$_3$O$_4$, and ZnO/Co$_3$O$_4$ composite (Fig. S4a–i†). Fig. 2d shows the Gr sheet-like morphology, which is wrinkled and folded over the edges. Subsequently, Fig. 2e and f show low and high-magnification FE-SEM micrographs of the ZnO/Co$_3$O$_4$@Gr nanocomposite. During the synthesis of ZnO/Co$_3$O$_4$@Gr, the regular morphology was disrupted, resulting in an uneven

Table 1 Overview of ZnO/Co$_3$O$_4$@Gr nanocomposite XPS results

Chemical element	Peak deconvolution	Binding energies (eV)	Interactions and oxidation states
Zn 2p	Zn 2p$_{3/2}$	1022.67	Zn^{2+}
	Zn 2p$_{1/2}$	1045.77	
Co 2p	Co 2p$_{3/2}$	780.41	Co^{3+} and Co^{2+}
		780.27	
		781.21	
	Co 2p$_{1/2}$	795.75	
		795.18	
		796.90	
O 1s		530.17	Co–O
		531.73	Zn–O
		533.14	H–O–H
C 1s		284.77	C–C/C=C (sp^2 hybridized)
		286.34	C–O–C
		288.71	C=O

This journal is © the Partner Organisations 2023
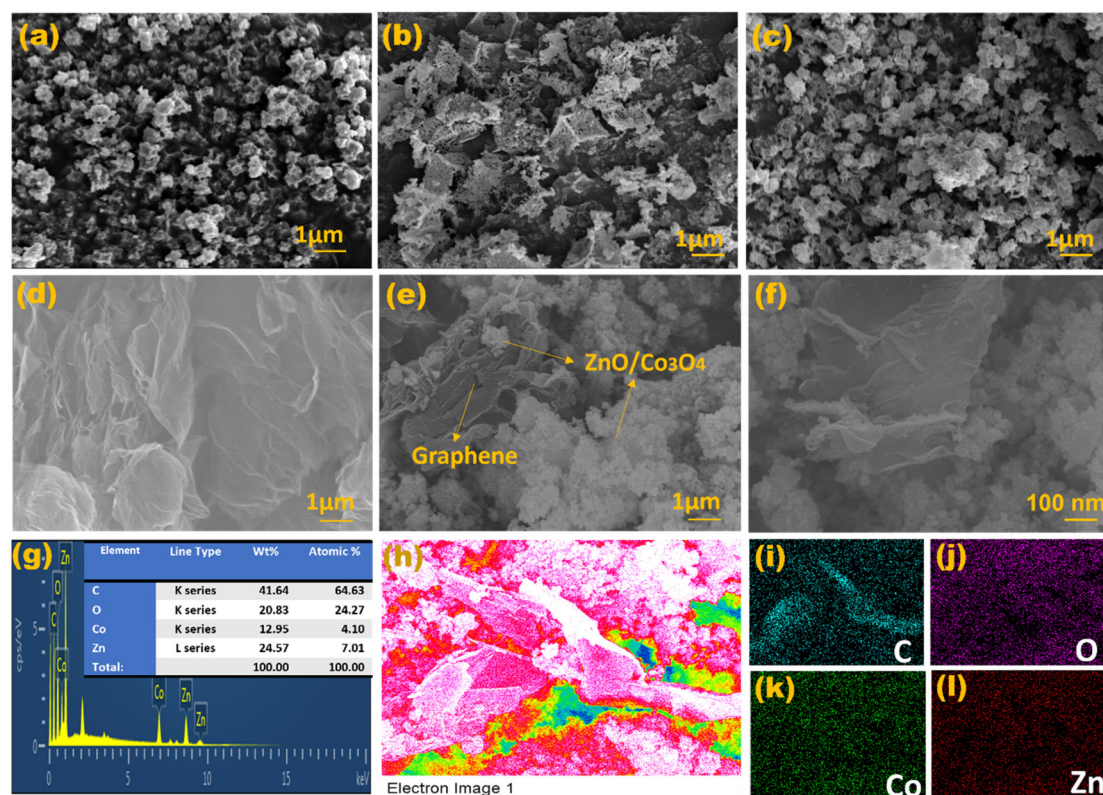
Inorg. Chem. Front., 2023, **10**, 4829–4844 | **4833**

Fig. 2 FE-SEM images of (a) ZnO, (b) Co₃O₄, (c) ZnO/Co₃O₄ composite, (d) Gr, and (e and f) low and high magnification images of the ZnO/Co₃O₄@Gr nanocomposite. (g) EDS spectrum of the ZnO/Co₃O₄@Gr nanocomposite. (h–l) EDS mapping analysis of the ZnO/Co₃O₄@Gr nanocomposite.

surface of Gr with smaller particles of ZnO/Co₃O₄. This suggests that the resulting material had a higher surface area than all ZIFs.[51] EDS spectra shown in Fig. 2g confirm the presence of the existing elements in the ZnO/Co₃O₄@Gr composite. EDS mapping study in Fig. 2h–l also reveals the presence of the elements C, O, Co, and Zn in the ZnO/Co₃O₄@Gr nanocomposite. FE-TEM images (Fig. 3a–d) at different magnifications clearly showed that small particle-sized ultrafine ZnO/Co₃O₄ particles were present on a transparent sheet-like structure of Gr. The high-resolution TEM (HRTEM) image in Fig. 3e showed lattice fringes with a lattice spacing of 0.217 nm for the (100) crystal plane and 0.283 nm for the (311) crystal plane, indicating the presence of oxides in the ZnO/Co₃O₄@Gr composite.[56] Selected area electron diffraction (SAED) patterns with obvious bright spots indicates the presence of the planes (111) (100) (311) (110) and (112) confirming the polycrystalline nature of the ZnO/Co₃O₄@Gr nanocomposite (Fig. 3f). Furthermore, the elemental distribution mapping from EDS (Fig. 3g–k) demonstrated the existence of components in the ZnO/Co₃O₄@Gr nanocomposite.

3.3. Electrochemical performance of ZnO/Co₃O₄@Gr

Following the successful demonstration of ZnO/Co₃O₄@Gr synthesis the electrochemical performance of the material was investigated. The conductivity and electron mobility of each

modified electrode was investigated using electrochemical impedance spectroscopy (EIS). Fig. 4a depicts the EIS spectra of bare GCE, ZnO/GCE, Co₃O₄/GCE, ZnO/Co₃O₄/GCE, Gr/GCE, and ZnO/Co₃O₄@Gr/GCE in 5 mM $[Fe(CN)_6]^{3-/4-}$ containing 0.1 M KCl using an applied amplitude potential of 0.005 V and the frequency range of 1 Hz–100 kHz. The Randles circuit, which was fitted using the data received from the EIS test results, is depicted in the inset of Fig. 4a, where R_{ct} denotes charge transfer resistance, R_s denotes electrolyte resistance, Z_w denotes the Warburg impedance, and C_{dl} denotes double-layer capacitance, respectively. The diameter of the semicircle exhibited in the Nyquist plot corresponds to the R_{ct} value, which demonstrates that the redox probe electron transfer rate kinetics occur at the electrode/electrolyte interface. The R_{ct} values of bare GCE, ZnO/GCE, Co₃O₄/GCE, ZnO/Co₃O₄/GCE, Gr/GCE, and ZnO/Co₃O₄@Gr/GCE were measured to be 619 Ω, 921 Ω, 837 Ω, 717 Ω, 465 Ω, and 371 Ω, respectively. The bare GCE shows lower impedance with a low R_{ct} value when compared to ZnO/GCE, Co₃O₄/GCE, and ZnO/Co₃O₄/GCE, which was due to the electrochemical activity of the solution interface and GCE surface. However, ZnO/Co₃O₄/GCE exhibits a greater R_{ct} and a larger impedance, indicating poor electrical conductivity, which slowed down the rate of electron transport. Likewise, ZnO/GCE, and Co₃O₄/GCE have larger R_{ct} compared to all other electrodes, which was due to the slow electron
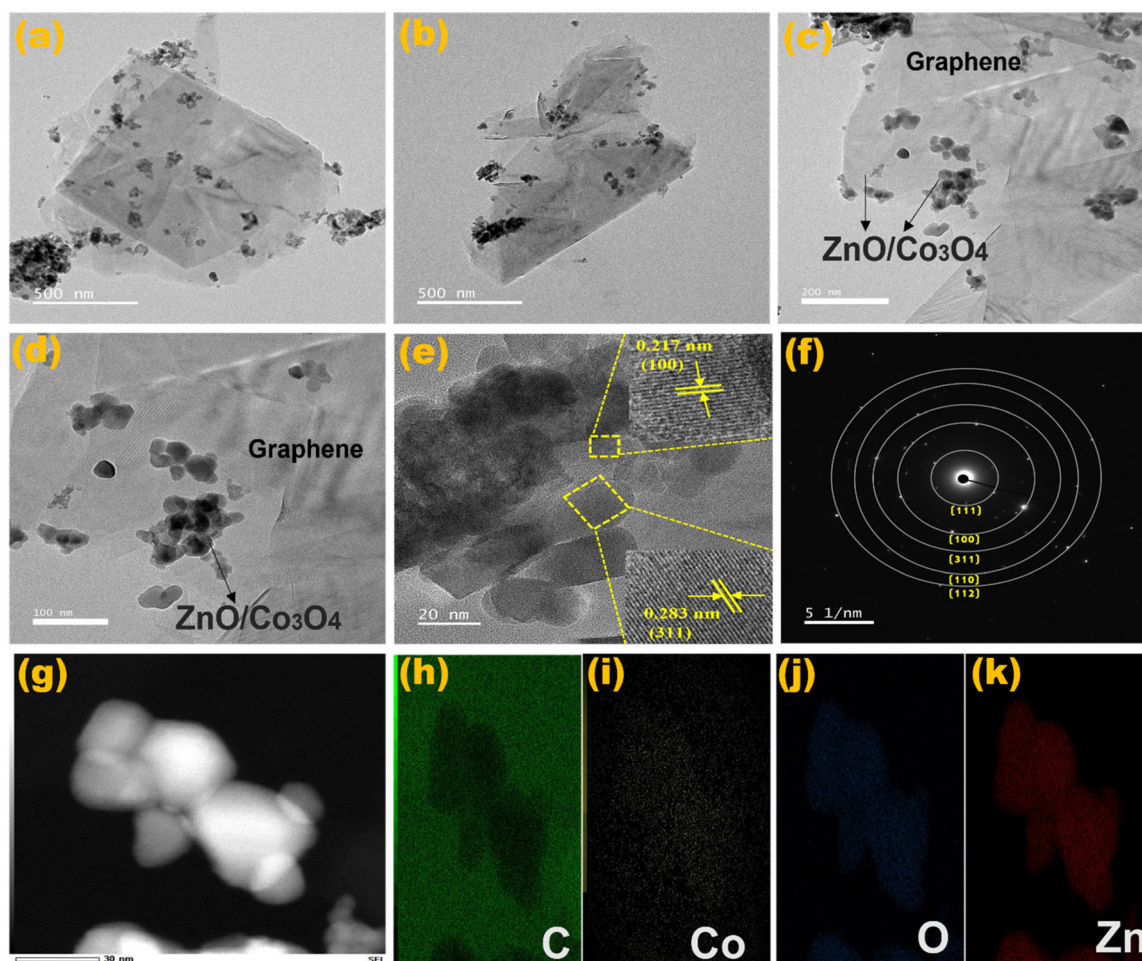
4834 | *Inorg. Chem. Front.*, 2023, **10**, 4829–4844

This journal is © the Partner Organisations 2023

Fig. 3 (a–d) FE-TEM images, (e) HR-TEM image, (f) SAED pattern, and (g–k) EDS mapping images of the ZnO/Co$_3$O$_4$@Gr nanocomposite.

transfer between the solution and the surface of the electrode. When Gr was added to the surface of GCE, R_{ct} (465 Ω) reduced in comparison with bare GCE, and on introducing Gr into ZnO/Co$_3$O$_4$ onto GCE further decreased R_{ct} to 371 Ω, suggesting that the electrical conductivity was significantly increased by the synergy effect between Gr and ZnO/Co$_3$O$_4$. EIS results show that the lowest R_{ct} value was attained with ZnO/Co$_3$O$_4$@Gr/GCE, demonstrating decent electrical conductivity and a rapid electron transfer rate.

Furthermore, the electrochemical behavior of modified electrodes was examined using cyclic voltammetry (CV) in 5 mM [Fe(CN)$_6$]$^{3-/4-}$/0.1 M KCl as shown in Fig. 4b. The CV analysis results demonstrate that ZnO/Co$_3$O$_4$@Gr/GCE has a greater peak current response (I_{pa}/I_{pc} = 15.52 μA/−16.19 μA) lower peak to peak separation potential (ΔE_p = 0.095 V), indicating good redox behavior with the redox probe [Fe(CN)$_6$]$^{3-/4-}$. The ΔE_p values of Gr/GCE, bare GCE, ZnO/Co$_3$O$_4$/GCE, Co$_3$O$_4$/GCE, and ZnO/GCE were 0.105, 0.165, 0.234, 0.309, and 0.323 V, respectively. These comparisons imply that the addition of Gr and ZnO/Co$_3$O$_4$ improves the feasibility of redox reactions at ZnO/Co$_3$O$_4$@Gr/GCE. These findings were corroborated by EIS measurements. Fig. 4c shows the electron transfer

kinetics of ZnO/Co$_3$O$_4$@Gr/GCE at various scan rates based on the CV analysis. The obtained redox peak current increased gradually with increased scan rates from 10 to 100 mV s^{-1}, indicating the diffusion-controlled kinetics of the proposed electrode. The corresponding linear plot of $v^{1/2}$ *vs.* peak currents (I_{pa}/I_{pc}) is shown in Fig. 4d. Meanwhile, Fig. S5a–d† shows the different scan rates obtained for Gr/GCE, ZnO/Co$_3$O$_4$/GCE, Co$_3$O$_4$/GCE, and ZnO/GCE, and their corresponding linearity plots are displayed in the insets of Fig S5a–d.† To calculate the electrochemical active surface area (EASA) of the modified electrodes, the Randles–Sevcik equation[57] (1) was applied.

$$I_p = (2.69 \times 10^5)n^{3/2}D^{1/2}Av^{1/2}C \tag{1}$$

where 'I_p' signifies the peak current (I_{pa}/I_{pc}), 'n' signifies the number of electrons involved in the rate-determining step (n = 1), 'D' signifies the diffusion coefficient (cm^2 s^{-1}), 'A' signifies the active surface area of the electrode (cm^2), and 'v' and 'C' signify the scan rate (mV s^{-1}) and concentration (mol cm^{-3}) of the redox probe [Fe(CN)$_6$]$^{3-/4-}$, respectively. The calculated EASA values of ZnO/Co$_3$O$_4$@Gr/GCE, Gr/GCE, ZnO/Co$_3$O$_4$/GCE, Co$_3$O$_4$/GCE, and

This journal is © the Partner Organisations 2023

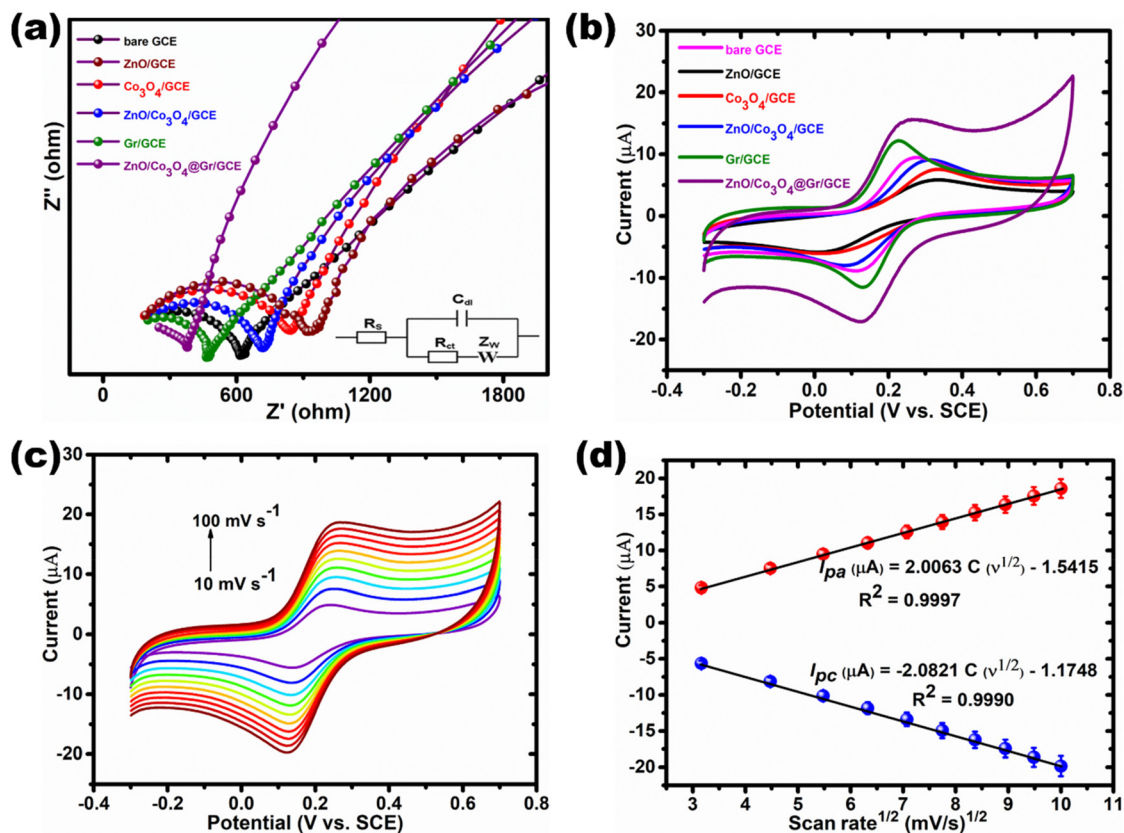*Inorg. Chem. Front.*, 2023, **10**, 4829–4844 | **4835**

Fig. 4 (a) EIS spectra and (b) CV analysis of bare GCE, ZnO/GCE, Co_3O_4/GCE, ZnO/Co_3O_4/GCE, Gr/GCE, and ZnO/Co_3O_4@Gr/GCE in 5 mM $[Fe(CN)_6]^{-3/-4}$ containing 0.1 M KCl. (c) CV curves at various scan rates from 10 to 100 mV s^{-1} at ZnO/Co_3O_4@Gr/GCE. (d) Linear plot of $v^{1/2}$ vs. redox peak currents (I_{pa}/I_{pc}).

ZnO/GCE were 0.41, 0.36, 0.29, 0.22, and 0.17 cm^2, respectively. The larger EASA, decreased resistance, and peak separation of the ZnO/Co_3O_4@Gr/GCE modified electrode demonstrate enhanced electrocatalytic activity for AFZ sensing.

3.4. Electrochemical behavior of AFZ on ZnO/Co_3O_4@Gr/GCE

To fully understand the electrochemical behavior of the newly developed sensor, we investigated various aspects of its development process, including the effect of modifier, pH, and scan rate. By taking advantage of the superior electrical conductivity of ZnO/Co_3O_4@Gr/GCE, we aimed to assess whether this electrode could be employed for the detection of AFZ. Fig. S6† shows the electrochemical performance of ZnO/GCE, Co_3O_4/GCE, and ZnO/Co_3O_4/GCE towards the detection of 1 mM AFZ. These electrodes displayed inadequate responses with lower oxidation peak currents, indicating poor conductivity and limited electrode surface area. On the other hand, Fig. 5a displays the CVs of bare and modified electrodes in 0.1 M PBS (pH 7.0) in the presence of 1 mM AFZ at a scan rate of 100 mV s^{-1}. It can be seen that the bare GCE exhibited the lowest oxidation peak current response (I_{pa} = 14.51 μA) compared to other modified electrodes, indicating that electron migration was hindered. Whereas Gr/GCE (I_{pa} = 26.89 μA) and ZnO/Co_3O_4@Gr/GCE (I_{pa} = 55.29 μA) showed noticeably higher

current responses, demonstrating that Gr can improve the electronic conductivity of ZnO/Co_3O_4. Interestingly, the ZnO/Co_3O_4@Gr/GCE nanocomposite electrode showed a maximum oxidation peak current response compared to the bare GCE (Fig. 5b). This was caused by the synergistic interaction and large electrochemically active surface area of the nanocomposite, that increased the oxidation peak current of AFZ.

To further study the antifouling properties of ZnO/Co_3O_4@Gr/GCE, CV was performed at a consistent scan rate of 100 mV s^{-1} with various AFZ concentrations (0 to 200 μM) in 0.1 M PBS (pH 7.0). As shown in Fig. 5c, the addition of AFZ led to a linear increase in peak current values, and the resulting calibration curve showed good linearity (inset of Fig. 5c) with the linear regression equation I_{pa} (μA) = 0.285 C_{AFZ} [μM] + 16.595, R^2 = 0.9971. These results demonstrated the strong antifouling activity of ZnO/Co_3O_4@Gr/GCE for the detection of AFZ. The pH of the solution may have impacted the behavior of the analyte and the rate of electron transport toward the nanocomposite electrode. The effect of pH on the electrochemical reaction toward 1 mM AFZ with ZnO/Co_3O_4@Gr/GCE was investigated using CV response at various pH levels (ranging from pH 5.0 to pH 9.0) at a scan rate of 100 mV s^{-1}. As shown in Fig. 5d, the peak current intensity increased as the pH of the electrolyte increased from 5.0 to 7.0, followed by
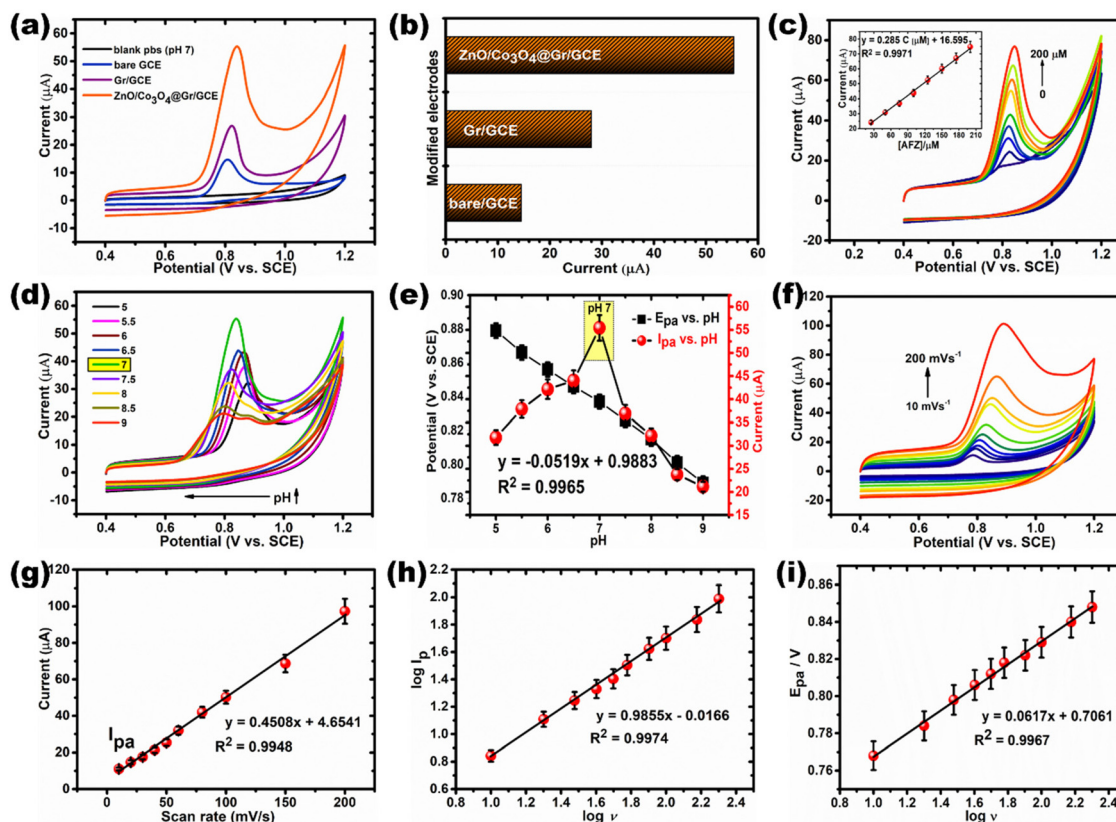
4836 | *Inorg. Chem. Front.*, 2023, **10**, 4829–4844

This journal is © the Partner Organisations 2023

Fig. 5 (a) CV curves of blank PBS (without AFZ), bare GCE, Gr/GCE, and ZnO/Co$_3$O$_4$@Gr/GCE in 1 mM AFZ containing 0.1 M PBS (pH 7.0). (b) Bar graphs of different modified electrodes *vs.* I_{pa}. (c) CV curves with increasing AFZ concentrations from 0 to 200 µM at ZnO/Co$_3$O$_4$@Gr/GCE in pH 7.0. Inset: the corresponding calibration plot of various AFZ concentrations *vs.* I_{pa}. (d) CV curves of 1 mM AFZ at various pH ranges from 5 to 9. (e) The calibration plot of the various pH *vs.* E_{pa} and I_{pa}. (f) CV curves for various scan rates ranging from 10 to 200 mV s^{-1} in the presence of 1 mM AFZ. The plots show the relationship between the peak current *vs.* scan rate (g), log current *vs.* log scan rate (h) and log scan rate *vs.* anodic peak potential (i).

a subsequent decrease from pH 7.0 to pH 9.0. Additionally, the peak potentials in the CV curves show a slight shift in the direction of the negative potential, which may be explained by variations in the acid–base protonation functions in the AFZ molecules.[58] The electro-oxidation of AFZ was successful at pH 7.0 due to the formation of a sharp, strong peak with good resolution. The plot of the peak current *vs.* various pH values (Fig. 5e) demonstrated that the maximum AFZ oxidation peak current was observed at pH 7.0, which was used throughout the experiment. The plot of E_{pa} *vs.* pH (Fig. 5e) revealed that the oxidation peak potential (E_{pa}) was linearly correlated with the various pH values, with the linear equation, $E_{pa} = -0.051$ C_{AFZ} (pH) + 0.988, $R^2 = 0.9965$. The slope value was close to the Nernstian theoretical value of -0.059 V against pH,[59] indicating that the electro-oxidation of AFZ involves an equal number of electrons and protons. These findings are consistent with the mechanism of the AFZ electro-oxidation reaction, as illustrated in Scheme 2.
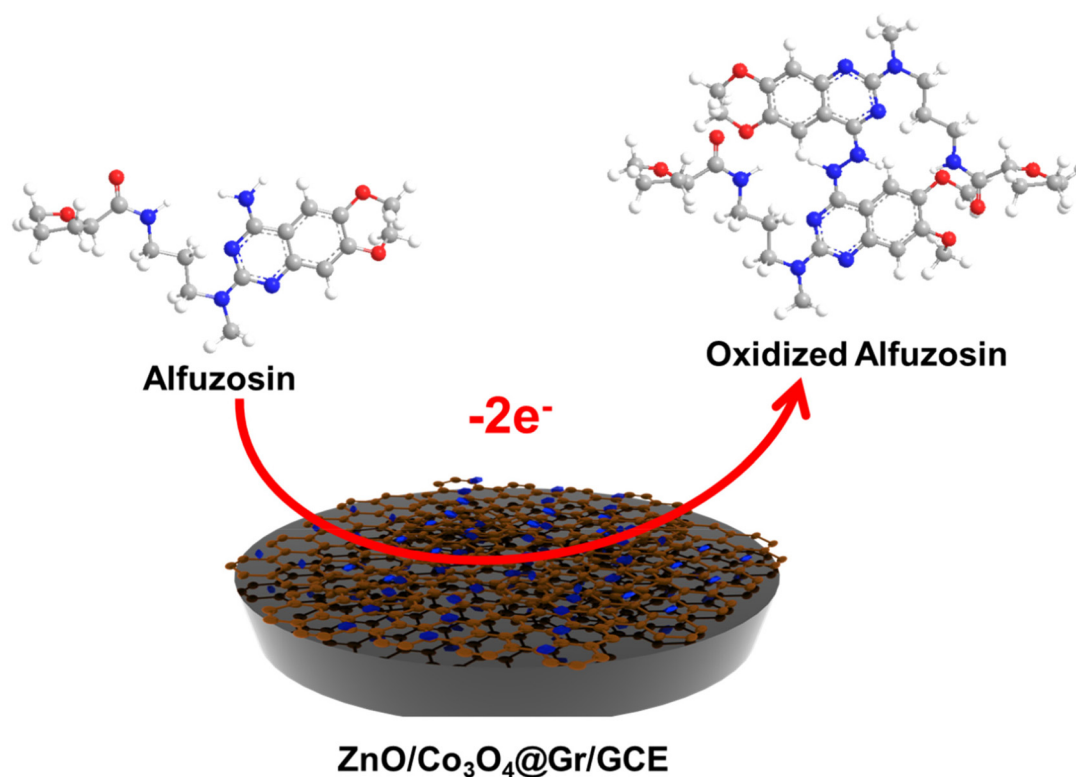
The influence of the scan rate (ν) on the electrochemical response of 1 mM AFZ on ZnO/Co$_3$O$_4$@Gr/GCE was also examined using CV at different scan rates. As shown in Fig. 5f, increasing the scan rates from 10 to 200 mV s^{-1} resulted in an increase in the oxidation peak currents of AFZ, with the anodic peak

potential gradually shifting towards higher values. A linear plot of various scan rates against I_{pa} is shown in Fig. 5g, using the associated linear regression equation, I_{pa} (µA) = 0.450 C_{AFZ} ν (mV s^{-1}) + 4.654, $R^2 = 0.9948$. These results indicate an adsorption-controlled AFZ system on the surface of ZnO/Co$_3$O$_4$@Gr/GCE. $\log I_p$ was also linear against $\log \nu$ (Fig. 5h), with the corresponding linear equation, $\log I_{pa}$ (µA) = 0.985 C_{AFZ} $\log \nu$ (mV s^{-1}) − 0.016, $R^2 = 0.9974$. A slope of 1.00 is expected for an ideal response of surfaces, and the observed slope of 0.98 confirms that the AFZ electro-oxidation reaction is adsorption-controlled kinetics.[13] The electrochemical kinetic parameters for an irreversible electrochemical process were calculated according to the following Laviron eqn (2) and (3).[60,61]

$$E_p = E° + (2.303RT/(1 - \alpha nF)) \log \nu + (2.303RT/(1 - \alpha nF)) \log(nF(1 - \alpha)/RTk_s) \quad (2)$$

$$\text{Log } k_s = \alpha \log(1 - \alpha) + (1 - \alpha) \log \alpha - \log(RT/nF\nu) - \alpha (1 - \alpha) nF\Delta E_p/2.3RT \quad (3)$$

where the variables such as $E°$, α, k_s, n, and ν denotes the formal potential, electron transfer coefficient, standard electron transfer

This journal is © the Partner Organisations 2023

Inorg. Chem. Front., 2023, **10**, 4829–4844 | **4837**

Alfuzosin

Oxidized Alfuzosin

-2e⁻

ZnO/Co₃O₄@Gr/GCE

Scheme 2 The possible electrochemical oxidation reaction of AFZ at ZnO/Co₃O₄@Gr/GCE.

rate constant, number of electrons involved in a reaction, and scan rate respectively, while the remaining R, T, and F values are constant. The peak potentials (E_{pa}) showed good linearity against the logarithm of scan rates (Fig. 5i) and the corresponding linear regression equation is E_{pa} (V) = 0.061 C_{AFZ} (log v) + 0.706, R^2 = 0.9967. Subsequently, the slope value of log v $vs.$ E_{pa} was used to
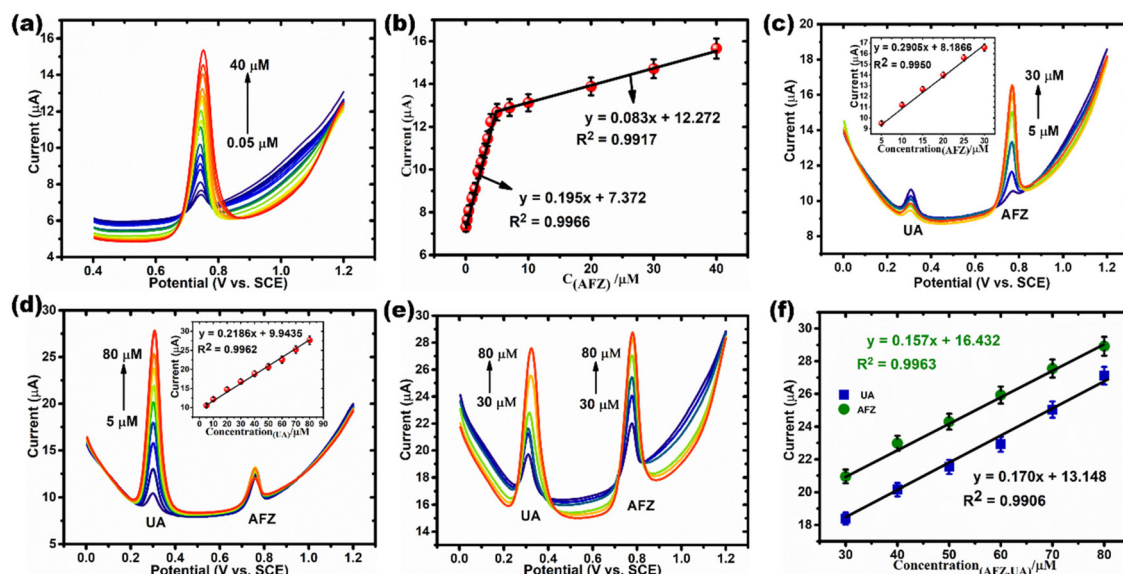

Fig. 6 (a) DPV curves of the ZnO/Co₃O₄@Gr/GCE obtained at the various AFZ concentrations ranging from 0.05 to 40 μM in the presence of 0.1 M PBS (pH 7.0). (b) Calibration plot of increasing concentrations of AFZ $vs.$ I_{pa}. (c) DPV curves of ZnO/Co₃O₄@Gr/GCE containing various AFZ concentrations from 5 to 30 μM in the presence of 1 mM UA. Inset: the corresponding calibration plot of various AFZ concentrations $vs.$ I_{pa}. (d) DPV curves of ZnO/Co₃O₄@Gr/GCE containing various UA concentrations from 5 to 80 μM in the presence of 1 mM AFZ. Inset: the corresponding calibration plot of various UA concentrations $vs.$ I_{pa}. (e) DPV curves of ZnO/Co₃O₄@Gr/GCE containing various concentrations of AFZ and UA from 30 to 80 μM in 0.1 M PBS (pH 7.0). (f) The corresponding calibration plot of various concentrations of AFZ and UA $vs.$ I_{pa}.

4838 | *Inorg. Chem. Front.*, 2023, **10**, 4829–4844

This journal is © the Partner Organisations 2023

calculate 'α' (0.54) and 'n' (1.96, equivalent to 2). Using eqn (2), 'k_s' was estimated to be 0.73 s^{-1}.

4. Analytical performance of the sensor

4.1. Calibration curve and selective detection

The response of the fabricated sensor to AFZ electro-oxidation was evaluated using a differential pulse voltammetry (DPV) approach that was sensitive, accurate, and reliable. The experimental variables that influence the DPV responses were optimized for AFZ in 0.1 M PBS (pH 7.0), such as pulse amplitude, pulse period, potential increment, pulse width, and sampling width. The ideal value of each parameter was chosen to

achieve the highest peak current and the best signal resolution. The optimal values for these variables were found to be: pulse amplitude = 0.05 V, pulse period = 0.5 s, potential increment = 0.004 V, pulse width = 0.05 s, and sampling width = 0.016 s. Fig. 6a shows the DPV analysis of AFZ on ZnO/Co$_3$O$_4$@Gr/GCE. The synergistic activity and non-covalent contact between ZnO/Co$_3$O$_4$ and Gr, which enhances the electrochemical performance for AFZ electro-oxidation, resulted in a progressive increase in the intensity of the peak current (I_{pa}). The calibration plot of AFZ concentrations (ranging from 0.05 to 40 μM) *versus* I_{pa} is shown in Fig. 6b, which shows two linear regions. Lower concentrations caused a very quick response because AFZ molecules were rapidly transferred to the electrode surface, while the larger concentrations caused a slower response. Therefore, two linear regions were obtained because of this irregular response.[62] The linear range of the lower concentrations was obtained between 0.05 and 4.0 μM, and the corresponding regression equation is I_{pa} (μA) = 0.195 C_{AFZ} [μM] + 7.372, R^2 = 0.9966. The linear range of higher concentrations was achieved between 5.0 and 40 μM, and the appropriate regression equation is I_{pa}(μA) = 0.083 C_{AFZ} [μM] + 12.272, R^2 = 0.9917. The limit of detection (LOD) value was found to be 0.004 μM, using the relationship 3S/m, where 'S' represents the standard deviation and 'm' represents the slope.[63] A comparison of the present fabricated sensor with previously reported AFZ sensors is shown in Table 2.[3,11,13,64,65]

One of the primary goals of this research is to investigate the ability of the newly constructed sensor in the selective detection of AFZ in the presence of UA. The sensor's well-defined DPV curves for the selective detection of AFZ and UA

Table 2 Comparison of the linear range and LOD for AFZ determination using various methods

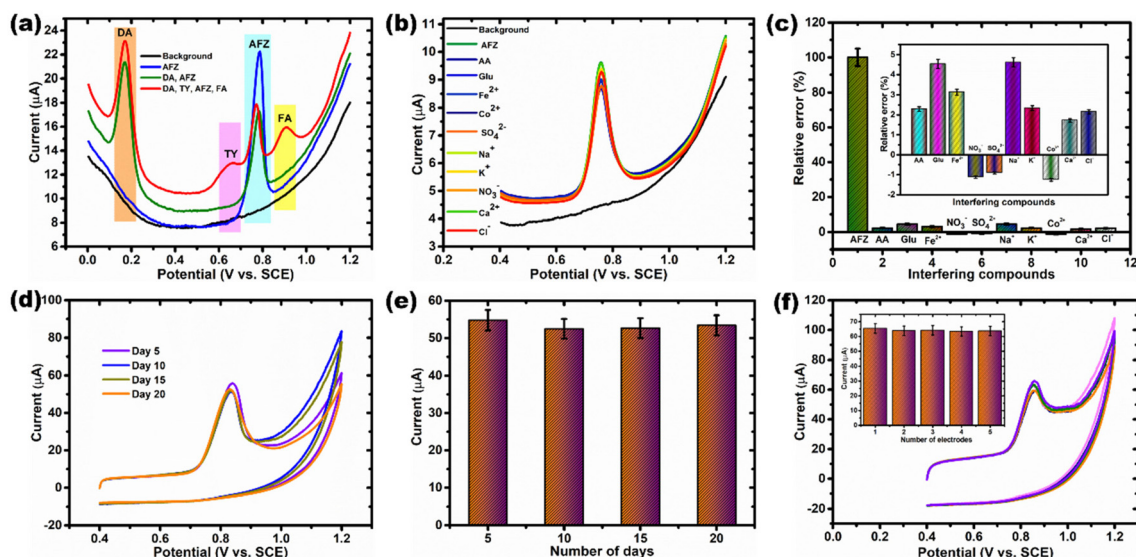| Method		Linear range (μM)	LOD (μM)	Ref.
CV, DPV, LSV and SWV at GCE		0.6–100	0.156	11
Potentiometric method using modified carbon paste electrodes (MCPEs)	Electrode-I	10–10 000	9.6	64
	Electrode-IV	10–10 000	9.7	
RP-HPLC		—	8.014	65
Colorimetric estimation		25–300	6.130	3
DPV and amperometry at MWCNT/CILE		0.02–90 and 10–100	0.0041	13
DPV at ZnO/Co$_3$O$_4$@Gr/GCE		0.05–40	0.004	This work

Fig. 7 (a) DPV curves of the ZnO/Co$_3$O$_4$@Gr/GCE obtained for 1 mM AFZ in 0.1 M PBS (pH 7.0) at various biologically active compounds and (b) some selected interfering species and (c) the bar plot of oxidation peak currents *vs.* interfering species. (d) CV responses for the stability of ZnO/Co$_3$O$_4$@Gr/GCE for 20 days. (e) The corresponding bar diagram for oxidation peak current *vs.* number of days run the experiment. (f) CV responses for five independent ZnO/Co$_3$O$_4$@Gr/GCEs and the inset the corresponding bar graph for oxidation current *vs.* five different modifies electrodes. All the above tests were performed in 0.1 M PBS (pH 7.0) containing 1 mM AFZ.

This journal is © the Partner Organisations 2023

Inorg. Chem. Front., 2023, **10**, 4829–4844 | **4839**

in 0.1 M PBS (pH 7.0) are presented in Fig. 6c and d. The peak currents of AFZ and UA steadily increased with an increasing concentration of AFZ (from 5 to 30 µM) and UA (from 5 to 80 µM), respectively, whereas the peak currents of other molecules at fixed concentrations remained unchanged. The insets of Fig. 6c and d show the calibration curves for AFZ and UA with the linear regression equations I_{pa} (µA) = 0.290 C_{AFZ} [µM] + 8.186, R^2 = 0.9950 and I_{pa} (µA) = 0.218 C_{UA} [µM] + 9.943, R^2 = 0.9962. The simultaneous detection of AFZ and UA with varying concentrations ranging from 30 to 80 µM was also conducted. Fig. 6e depicts well-resolved DPV curves with the intensity of peak currents gradually increasing with the synchronous addition of AFZ and UA. The calibration plots of AFZ and

UA, along with the linear regression equations I_{pa} (µA) = 0.157 C_{AFZ} [µM] + 16.432, R^2 = 0.9963 and I_{pa} (µA) = 0.170 C_{UA} [µM] + 13.148, R^2 = 0.9906, are given in Fig. 6f. The sensor demonstrated improved analytical performance, with a lower detection limit and excellent selectivity.

4.2. Effect of excipients on AFZ detection, stability, and reproducibility

In practical applications, it is critical to evaluate the interference of excipients such as some commonly used biological metabolites and inorganic compounds toward the detection of AFZ. Thus, we employed the DPV technique to evaluate the selectivity of our sensor by adding biologically active com-
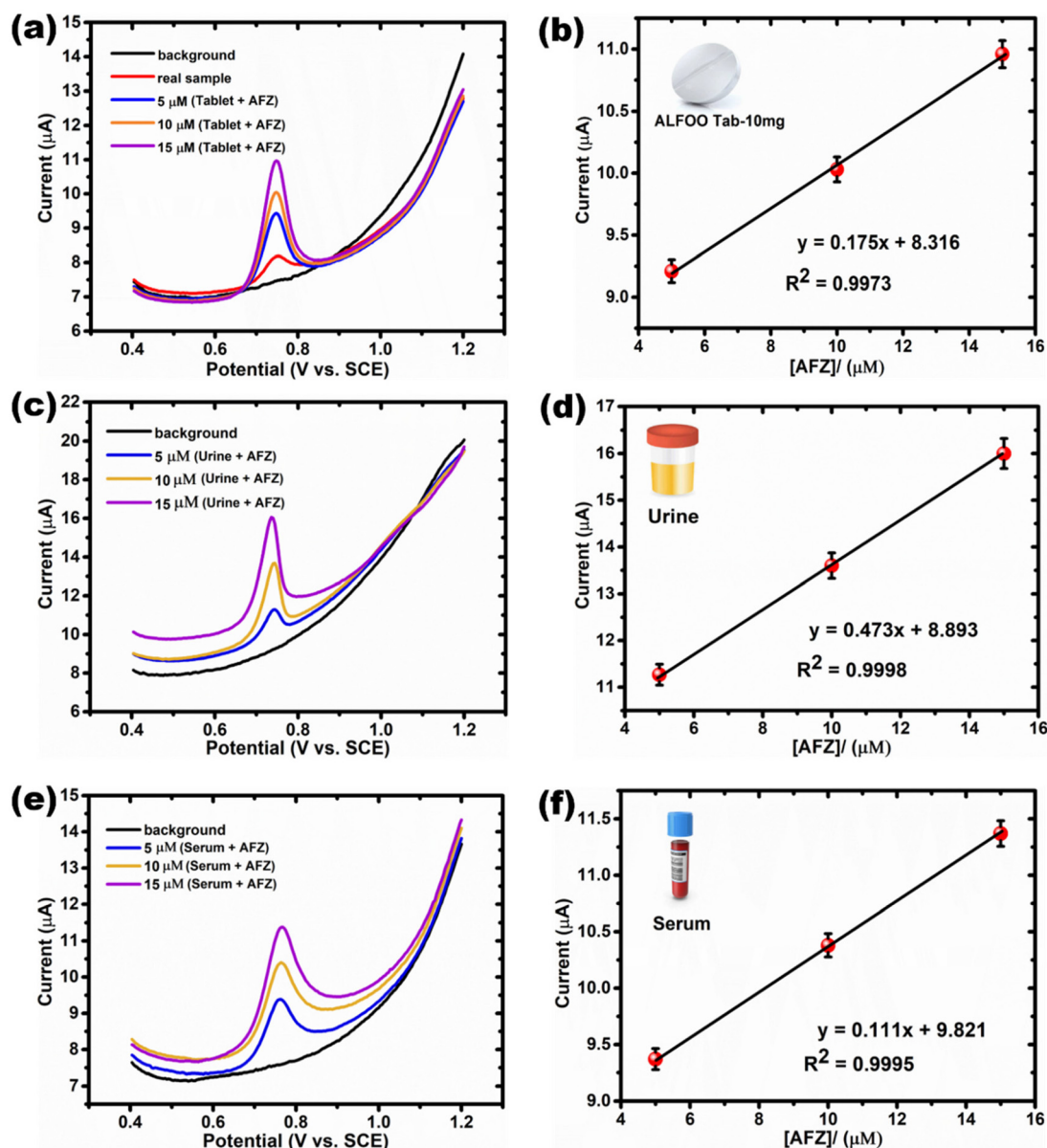

Fig. 8   (a, c and e) DPV curves of ZnO/Co$_3$O$_4$@Gr/GCE obtained for the tablets, urine, and serum real samples added to standard AFZ concentrations in 0.1 M PBS (pH 7.0) and (b, d and f) the corresponding linear plots between peak currents *vs.* various AFZ concentrations of the tablets, urine, and serum samples.

pounds, such as dopamine (DA), tyrosine (TY), and folic acid (FA), in 10-fold excess to 0.1 M PBS (pH 7.0) in the presence of 1 mM AFZ, as shown in Fig. 7a. The results revealed that the sensor did not exhibit a significant peak potential change, indicating that biologically active chemicals did not interfere with the detection of AFZ. We also examined the effect of selected foreign species interfering with 1 mM AFZ in the presence of 0.1 M PBS (pH 7.0) as shown in Fig. 7b. These species included cations (Fe^{2+}, Co^{2+}, Na^+, K^+, and Ca^{2+}), anions (SO_4^{2-}, NO_3^-, and Cl^-), ascorbic acid (AA), and glucose (Glu) in a 10-fold excess concentration. The oxidation peak current did not change significantly with the addition of interfering substances, as depicted in Fig. 7b and the bar graph of the oxidation current response against various interfering species displayed a relative error of less than 5% (Fig. 7c). This demonstrates the $ZnO/Co_3O_4@Gr/GCE$ sensor's strong selectivity for the detection of AFZ. Furthermore, we examined the electrochemical long-term stability of the sensor in 0.1 M PBS (pH 7.0) with 1 mM AFZ at a scan rate of 100 mV s^{-1} for 20 days using the CV approach (Fig. 7d). The study was performed every five days after the electrode was stored in a refrigerator at 4 °C. The sustained peak current was 95.6% of its initial peak current, as shown in the bar graph in Fig. 7e, demonstrating the exceptional durability of the $ZnO/Co_3O_4@Gr/GCE$ sensor. Finally, we investigated the reproducibility of the suggested method using five different freshly prepared $ZnO/Co_3O_4@Gr/GCEs$ and the CV approach (Fig. 7f). The obtained results displayed a relative standard deviation (RSD) of 3.2% (inset of Fig. 7f), indicating that the $ZnO/Co_3O_4@Gr/GCE$ has excellent reproducibility.

4.3. Real sample analysis

Considering the sensitivity and selectivity of the fabricated sensor, we have evaluated its potential for detecting AFZ in real samples. We used the DPV approach to test the real-time applicability of our proposed $ZnO/Co_3O_4@Gr/GCE$ sensor by the standard addition method in AFZ-containing pharmaceutical tablets, AFZ-free human serum, and urine samples (Fig. 8a, c and e). The experimental strategy for preparing real samples utilized in this method is briefly discussed in the ESI section (S4).† As shown in Fig. 8a, c, and e, we observed a DPV response to the direct addition of the tablet, human urine, and human serum samples, as well as AFZ spiked with increasing concentrations ranging from 5 to 15 μM. Table S1† presents the estimated recoveries for the tablets, human urine, and human serum samples. Fig. 8b, d, and f demonstrate the linear relationship between the peak current and the AFZ concentration of the actual samples. These results demonstrate that the fabricated $ZnO/Co_3O_4@Gr/GCE$ sensor has acceptable recoveries for the monitoring of AFZ in real samples.

5. Conclusion

We have presented a coprecipitation method for synthesizing ZnO/Co_3O_4 derived from a MOF, which was subsequently deco-

rated on graphene using a simple ultrasonication method. The resulting $ZnO/Co_3O_4@Gr$ nanocomposite was extensively characterized by a variety of spectroscopic techniques, including XRD, XPS, ATR-IR, FE-SEM, FE-TEM, and EDS with elemental mapping. We also investigated its electrochemical properties using CV, EIS, and DPV methods. Our results showed that the $ZnO/Co_3O_4@Gr$ modified GCE had excellent electroanalytical characteristics, and we successfully used it to detect the α1-AR antagonist AFZ for the first time. The DPV results were interesting in that they demonstrated a good linear range of 0.05–40 μM with a low LOD of 0.004 μM for AFZ detection, which is a significant improvement over other reported methods. Furthermore, due to the synergistic effect of ZnO/Co_3O_4 and Gr, the sensor exhibited remarkable selectivity, anti-interference capability, storage stability, and reproducibility. Finally, we demonstrated the sensor's potential for real-time detection of AFZ in biological (urine and serum) and pharmaceutical (tablet) samples, with considerable recoveries. These results suggest that our low-cost, environmentally friendly sensor materials have great potential for future applications in the field of electrochemical sensing.

Conflicts of interest

There are no conflicts to declare.

Acknowledgements

References

1 M. J. Barry and C. G. Roehrborn, Benign prostatic hyperplasia, *Br. Med. J.*, 2001, **323**, 1042–1046.

2 J. J. M. C. H. de la Rosette, H. F. M. Karthaus, Ph. E. V. A. van Kerrebroeck, Th. de Boo and F. M. J. Debruyne, Research in "Prostatitis Syndromes": The Use of Alfuzosin (a New α(1)-Receptor-Blocking Agent) in Patients Mainly Presenting with Micturition Complaints of an Irritative Nature and Confirmed Urodynamic Abnormalities, *Eur. Urol.*, 1992, **22**, 222–227.

This journal is © the Partner Organisations 2023

Inorg. Chem. Front., 2023, **10**, 4829–4844 | **4841**

3 K. A. M. Attia, N. M. El-Abasawi and A. H. Abdelazim, Colorimetric estimation of alfuzosin hydrochloride in pharmaceutical preparation based on computational studies, *Anal. Methods*, 2016, **8**, 1798–1805.

4 S. Siroosbakht, S. Rezakhaniha, F. Namdari and B. Rezakhaniha, Is there relationship between serum uric acid levels and lower urinary tract symptoms, prostate volume, and PSA in men without cancer? A prospective population-based study, *Andrologia*, 2021, **53**, e14200.

5 B.-S. Hou, X.-Y. Xia, L.-J. Pan, B. Yang, Y. Shao, X.-J. Shang, B. Yao, Y.-X. Cui and Y.-F. Huang, Determination of uric acid in the expressed prostatic secretion of chronic prostatitis patients and its clinical significance, *Zhonghua Nankexue*, 2008, **14**, 245–247.

6 A. Salah Fayed, M. Abdel-Aaty Shehata, N. Y. Hassan and S. A. El-Weshahy, Validated HPLC and HPTLC stability-indicating methods for determination of alfuzosin hydrochloride in bulk powder and pharmaceutical formulations, *J. Sep. Sci.*, 2006, **29**, 2716–2724.

7 S. Ashour and M. Khateeb, Conductometric Titration Method for Determination of Alfuzosin Hydrochloride and Fexofenadine Hydrochloride Using Sodium Tetraphenylborate, *Can. Chem. Trans.*, 2013, 292–304.

8 M. E. B. Mohamed, E. Y. Frag and Y. M. G. Eldin, A validated potentiometric method for determination of alfuzosin hydrochloride in pharmaceutical and biological fluid samples, *J. Iran. Chem. Soc.*, 2020, **17**, 2257–2265.

9 S. Ashour, M. F. Chehna and R. Bayram, Spectrophotometric Determination of Alfuzosin HCl in Pharmaceutical Formulations with some Sulphonephthalein Dyes, *Int. J. Biomed. Sci.*, 2006, **2**, 273.

10 Y. Abbas, S. Ali, M. Basharat, W. Zou, F. Yang, W. Liu, S. Zhang, Z. Wu, N. Akhtar and D. Wu, Heteroatom-Doped Carbon Nanoparticle–Ionic Liquid Composites as Electrochemical Sensors for Uric Acid, *ACS Appl. Nano Mater.*, 2020, **11**, 11383–11390.

11 B. Uslu, Voltammetric Analysis of Alfuzosin HCl in Pharmaceuticals, Human Serum and Simulated Gastric Juice, *Electroanalysis*, 2002, **14**, 866–870.

12 Z. Pourghobadi and R. Pourghobadi, Electrocatalytic Alfuzosin Oxidation on Electrochemically Oxidized Glassy Carbon Modified with Multiwalled Carbon Nanotubes and Nickel Oxide Nanoparticles, *J. Electrochem. Soc.*, 2019, **166**, B76–B83.

13 M. R. Baezzat, F. Banavand and F. Fasihi, Electrooxidation study and highly sensitive voltammetric determination of alfuzosin employing multi-walled carbon nanotubes and the ionic liquid 1-hexylpyridinium hexafluorophosphate nanocomposite sensor, *J. Mol. Liq.*, 2017, **233**, 391–397.

14 A. S. Agnihotri, A. Varghese and N. M, Transition metal oxides in electrochemical and bio sensing: A state-of-art review, *Appl. Surf. Sci. Adv.*, 2021, **4**, 100072.

15 A. V. Emeline, G. V. Kataeva, A. V. Panasuk, V. K. Ryabchuk, N. V. Sheremetyeva and N. Serpone, Effect of Surface Photoreactions on the Photocoloration of a Wide Band Gap Metal Oxide: Probing Whether Surface Reactions Are Photocatalytic, *J. Phys. Chem. B*, 2005, **109**, 5175–5185.

16 G. Mavroua, S. Galata, P. Tsipas, A. Sotiropoulos, Y. Panayiotatos and A. Dimoulas, Electrical properties of La_2O_3 and HfO_2/La_2O_3 gate dielectrics for germanium metal-oxide-semiconductor devices, *J. Appl. Phys.*, 2008, **103**, 014506.

17 Y. Xiong, W. Xu, Z. Zhu, Q. Xue, W. Lu, D. Ding and L. Zhu, ZIF-derived porous $ZnO-Co_3O_4$ hollow polyhedrons heterostructure with highly enhanced ethanol detection performance, *Sens. Actuators, B*, 2017, **253**, 523–532.

18 J. M. Xu and J. P. Cheng, The advances of Co_3O_4 as gas sensing materials: A review, *J. Alloys Compd.*, 2016, **686**, 753–768.

19 J. M. Gonçalves, D. P. Rocha, M. N. T. Silva, P. R. Martins, E. Nossol, L. Angnes, C. Sekhar Rout and R. A. A. Munoz, Feasible strategies to promote the sensing performances of spinel MCo_2O_4 (M = Ni, Fe, Mn, Cu and Zn) based electrochemical sensors: a review, *J. Mater. Chem. C*, 2021, **9**, 7852–7887.

20 R. Narayan, *Encyclopedia of Sensors and Biosensors*, Elsevier, 2023.

21 J. Ganesamurthi, R. Shanmugam, T.-W. Chen, S.-M. Chen, M. Balamurugan, Z.-W. Gan, M. R. Siddiqui, S. M. Wabaidur and M. A. Ali, NiO/ZnO binary metal oxide based electrochemical sensor for the evaluation of hazardous flavonoid in biological and vegetable samples, *Colloids Surf., A*, 2022, **647**, 129077.

22 X. Chen, Z. Wu, D. Liu and Z. Gao, Preparation of ZnO Photocatalyst for the Efficient and Rapid Photocatalytic Degradation of Azo Dyes, *Nanoscale Res. Lett.*, 2017, **12**, 143.

23 J. M. Gonçalves, P. R. Martins, D. P. Rocha, T. A. Matias, M. S. S. Julia, R. A. A. Munoz and L. Angnes, Recent trends and perspectives in electrochemical sensors based on MOF-derived materials, *J. Mater. Chem. C*, 2021, **9**, 8718.

24 E. H. Kwon, M. Kim, C. Y. Lee, M. Kim and Y. D. Park, Metal–Organic-Framework-Decorated Carbon Nanofibers with Enhanced Gas Sensitivity When Incorporated into an Organic Semiconductor-Based Gas Sensor, *ACS Appl. Mater. Interfaces*, 2022, **14**, 10637–10647.

25 S. A. Al Kiey and H. N. Abdelhamid, Metal-organic frameworks (MOFs)-derived Co_3O_4@N-doped carbon as an electrode materials for supercapacitor, *J. Energy Storage*, 2022, **55**, 105449.

26 L. Li, S. Han, S. Zhao, X. Li, B. Liu and Y. Liu, Chitosan modified metal–organic frameworks as a promising carrier for oral drug delivery, *RSC Adv.*, 2020, **10**, 45130–45138.

27 H. Liu, H. Wang, Q. Song, K. Küster, U. Starke, P. A. van Aken and E. Klemm, Assembling Metal Organic Layer Composites for High-Performance Electrocatalytic CO_2 Reduction to Formate, *Angew. Chem., Int. Ed.*, 2022, **61**, e202117058.

28 Y. Wang, Y. Wu, J. Xie and X. Hu, Metal–organic framework modified carbon paste electrode for lead sensor, *Sens. Actuators, B*, 2013, **177**, 1161–1166.

29 Y. Chen, N. Wang, W. Hu and S. Komarneni, In situ construction of porous Ni/Co-MOF@Carbon cloth electrode

4842 | *Inorg. Chem. Front.*, 2023, **10**, 4829–4844

This journal is © the Partner Organisations 2023

with honeycomb-like structure for high-performance energy storage, *J. Porous Mater.*, 2019, **26**, 921–929.

30 A. S. Rajpurohit, N. S. Punde and A. K. Srivastava, A dual metal organic framework based on copper-iron clusters integrated sulphur doped graphene as a porous material for supercapacitor with remarkable performance characteristics, *J. Colloid Interface Sci.*, 2019, **553**, 328–340.

31 X. Wang, J. Zhang, Y. Wei, T. Xing, T. Cao, S. Wu and F. Zhu, A copper-based metal–organic framework/graphene nanocomposite for the sensitive and stable electrochemical detection of DNA bases, *Analyst*, 2020, **145**, 1933–1942.

32 J. Lv, C. Zhang, S. Wang, M. Li and W. Guo, MOF-derived porous ZnO-Co$_3$O$_4$ nanocages as peroxidase mimics for colorimetric detection of copper(II) ions in serum, *Analyst*, 2021, **146**, 605–611.

33 W. Zhan, Q. Kuang, J. Zhou, X. Kong, Z. Xie and L. Zheng, Semiconductor@Metal–Organic Framework Core–Shell Heterostructures: A Case of ZnO@ZIF-8 Nanorods with Selective Photoelectrochemical Response, *J. Am. Chem. Soc.*, 2013, **135**, 1926–1933.

34 J. Wang, J. Zhao, J. Yang, J. Cheng, Y. Tan, H. Feng and Y. Li, An electrochemical sensor based on MOF-derived NiO@ZnO hollow microspheres for isoniazid determination, *Microchim. Acta*, 2020, **187**, 380.

35 C. Zhang, J. Ren, Y. Xing, M. Cui, N. Li, P. Liu, X. Wen and M. Li, Fabrication of hollow ZnO-Co$_3$O$_4$ nanocomposite derived from bimetallic-organic frameworks capped with Pd nanoparticles and MWCNTs for highly sensitive detection of tanshinol drug, *Mater. Sci. Eng., C*, 2020, **108**, 110214.

36 A. J. Jesu Amalraj, U. Narasimha Murthy and W. Sea-Fue, Ultrasensitive electrochemical detection of an antibiotic drug furaltadone in fish tissue with a ZnO-ZnCo$_2$O$_4$ self-assembled nano-heterostructure as an electrode material, *Microchem. J.*, 2021, **169**, 106566.

37 B. Li, J. Liu, Q. Liu, R. Chen, H. Zhang, J. Yu, D. Song, J. Li, M. Zhang and J. Wang, Core-shell structure of ZnO/Co$_3$O$_4$ composites derived from bimetallic-organic frameworks with superior sensing performance for ethanol gas, *Appl. Surf. Sci.*, 2019, **475**, 700–709.

38 Md. Rakibuddin and R. Ananthakrishnan, Porous ZnO/Co$_3$O$_4$ heteronanostructures derived from nano coordination polymers for enhanced gas sorption and visible light photocatalytic applications, *RSC Adv.*, 2015, **5**, 68117–68127.

39 A. K. Geim and K. S. Novoselov, The rise of graphene, *Nat. Mater.*, 2007, **6**, 183–191.

40 G. Venkataprasad, T. M. Reddy, A. L. Narayana, O. M. Hussain, T. V. Gopal and P. Shaikshavali, Hydrothermal synthesis of intertwining network structured TiO$_2$ nanocomposite: A promising material for the effective monitoring of dopamine and anodic performance in lithium-ion battery, *Synth. Met.*, 2020, **265**, 116403.

41 A. T. E. Vilian, B. Dinesh, M. Rethinasabapathy, S.-K. Hwang, C.-S. Jin, Y. S. Huh and Y.-K. Han, Hexagonal Co$_3$O$_4$ anchored reduced graphene oxide sheets for high-performance supercapacitors and non-enzymatic glucose sensing, *J. Mater. Chem. A*, 2018, **6**, 14367–14379.

42 C. Pettinari and A. Tombesi, MOFs for Electrochemical Energy Conversion and Storage, *Inorganics*, 2023, **11**, 65.

43 T. Ma, H. Li, J. G. Ma and P. Cheng, Application of MOF-based materials in electrochemical sensing, *Dalton Trans.*, 2020, **49**, 17121–17129.

44 K. Li, Y. Zhang, P. Wang, X. Long, L. Zheng, G. Liu, X. He and J. Qiu, Core-Shell ZIF-67@ZIF-8-derived multi-dimensional cobalt-nitrogen doped hierarchical carbon nanomaterial for efficient oxygen reduction reaction, *J. Alloys Compd.*, 2022, **903**, 163701.

45 G. Kaur, R. K. Rai, D. Tyagi, X. Yao, P.-Z. Li, X.-C. Yang, Y. Zhao, Q. Xu and S. K. Singh, Room-temperature synthesis of bimetallic Co–Zn based zeolitic imidazolate frameworks in water for enhanced CO$_2$ and H$_2$ uptakes, *J. Mater. Chem. A*, 2016, **4**, 14932–14938.

46 G. Venkataprasad, T. M. Reddy, A. L. Narayana, O. M. Hussain, P. Shaikshavali, T. V. Gopal and P. Gopal, A facile synthesis of Fe$_3$O$_4$-Gr nanocomposite and its effective use as electrochemical sensor for the determination of dopamine and as anode material in lithium ion batteries, *Sens. Actuators, A*, 2019, **293**, 87–100.

47 H. Dong Chul, R. Vinodh, C. V. V. M. Gopi, C. Deviprasath, H.-J. Kim and M. Yi, Effect of the cobalt and zinc ratio on the preparation of zeolitic imidazole frameworks (ZIFs): synthesis, characterization and supercapacitor applications, *Dalton Trans.*, 2019, **48**, 14808–14819.

48 A. D. Jagadale, V. S. Kumbhar, R. N. Bulakhe and C. D. Lokhande, Influence of electrodeposition modes on the supercapacitive performance of Co$_3$O$_4$ electrodes, *Energy*, 2014, **64**, 234–241.

49 D. Zhang, Z. Yang, Z. Wu and G. Dong, Metal-organic frameworks-derived hollow zinc oxide/cobalt oxide nanoheterostructure for highly sensitive acetone sensing, *Sens. Actuators, B*, 2019, **283**, 42–51.

50 P. Veerakumar, A. Sangili, S. M. Chen, V. Vinothkumar, S. Balu, S. T. Hung and K. C. Lin, Zinc and Sulfur Codoped Iron Oxide Nanocubes Anchored on Carbon Nanotubes for the Detection of Antitubercular Drug Isoniazid, *ACS Appl, Nano Mater.*, 2021, **4**, 4562–4575.

51 H. Zhu, J. Liu, Q. Zhang and J. Wei, High electrochemical performance of metal azolate framework-derived ZnO/Co$_3$O$_4$ for supercapacitors, *Int. J. Energy Res.*, 2020, **44**, 8654–8665.

52 V. Vinothkumar, R. Sakthivel, S. M. Chen, A. Sangili and T. H. Kim, Construction of Sr@Mn$_3$O$_4$/GO nanocomposite: a synergistic electrocatalyst for nitrofurantoin detection in biological and environmental samples, *Environ. Sci.: Nano*, 2023, **10**, 503–518.

53 Elizbit, U. Liaqat, Z. Hussain, M. M. Baig, M. A. Khan and D. Arif, Preparation of porous ZIF-67 network interconnected by MWCNTs and decorated with Ag nanoparticles for improved non-enzymatic electrochemical glucose sensing, *J. Korean Ceram. Soc.*, 2021, **58**, 598–605.

This journal is © the Partner Organisations 2023

Inorg. Chem. Front., 2023, **10**, 4829–4844 | **4843**

54 S. Wang, X. Ke, S. Zhong, Y. Lai, D. Qian, Y. Wang, Q. Wang and W. Jiang, Bimetallic zeolitic imidazolate frameworks-derived porous carbon-based materials with efficient synergistic microwave absorption properties: the role of calcining temperature, *RSC Adv.*, 2017, **7**, 46436–46444.

55 Y. Xiong, W. Liu, X. Qiao, X. Song, S. Wang, X. Zhang, X. Wang and J. Tian, Confined synthesis of 2D ultrathin ZnO/Co₃O₄ nanomeshes heterostructure for superior tri-ethylamine detection at low temperature, *Sens. Actuators, B*, 2021, **346**, 130486.

56 W. Yan, H. Xu, M. Ling, S. Zhou, T. Qiu, Y. Deng, Z. Zhao and E. Zhang, MOF-Derived Porous Hollow Co₃O₄@ZnO Cages for High-Performance MEMS Trimethylamine Sensors | ACS Sensors, *ACS Sens.*, 2021, **6**, 2613–2621.

57 V. Vinothkumar, G. V. Prasad, S.-M. Chen, A. Sangili, S.-J. Jang, H. C. Lim and T. H. Kim, One-step synthesis of calcium-doped copper oxide nanoparticles as an efficient bifunctional electrocatalyst for sensor and supercapacitor applications, *J. Energy Storage*, 2023, **59**, 106415.

58 N. P. Shetti, D. S. Nayak, S. J. Malode, R. R. Kakarla, S. S. Shukla and T. M. Aminabhavi, Sensors based on ruthenium-doped TiO₂ nanoparticles loaded into multi-walled carbon nanotubes for the detection of flufenamic acid and mefenamic acid, *Anal. Chim. Acta*, 2019, **1051**, 58–72.

59 T. V. Gopal, T. M. Reddy, G. Venkataprasad, P. Shaikshavalli and P. Gopal, Rapid and sensitive electro-chemical monitoring of paracetamol and its simultaneous resolution in presence of epinephrine and tyrosine at GO/poly (Val) composite modified carbon paste electrode, *Colloids Surf., A*, 2018, **545**, 117–126.

60 E. J. J. Laviron, General expression of the linear potential sweep voltammogram in the case of diffusionless electro-chemical systems, *J. Electroanal. Chem. Interfacial Electrochem.*, 1979, **101**, 19–28.

61 G. Venkata Prasad, V. Vinothkumar, S. J. Jang, D. Eun Oh and T. H. Kim, Multi-walled carbon nanotube/graphene oxide/poly(threonine) composite electrode for boosting electrochemical detection of paracetamol in biological samples, *Microchem. J.*, 2023, **184**, 108205.

62 S. Kubendhiran, R. Sakthivel, S.-M. Chen, R. Anbazhagan and H.-C. Tsai, A novel design and synthesis of ruthenium sulfide decorated activated graphite nanocomposite for the electrochemical determination of antipsychotic drug chlor-promazine, *Composites, Part B*, 2019, **168**, 282–290.

63 G. V. Prasad, S. J. Jang, Y. C. Sekhar, T. M. Reddy, L. S. Sarma, H. B. Kim and T. H. Kim, Fine-tuning of Pd–CeO₂/rGO nanocomposite: A facile synergetic strategy for effective electrochemical detection of dopamine in pharmaceutical and biological samples, *J. Electroanal. Chem.*, 2023, **941**, 117544.

64 A. A. Hasseba, G. G. Mohameda and S. E. Elasherya, Potentiometric determination of alfuzosin hydrochloride in pharmaceutical preparations and biological fluids using modified carbon paste electrodes, *J. Basic Environ. Sci.*, 2019, **6**, 318–323.

65 G. M. Hadad, S. Emara and W. M. M. Mahmoud, Development and validation of a stability-indicating RP-HPLC method for the determination of paracetamol with dantrolene or/and cetirizine and pseudoephedrine in two pharmaceutical dosage forms, *Talanta*, 2009, **79**, 1360–1367.

4844 | *Inorg. Chem. Front.*, 2023, **10**, 4829–4844

This journal is © the Partner Organisations 2023